Front. Chem. Sci. Eng. 2023, 17(5): 516−524
https://doi.org/10.1007/s11705-022-2238-z

RESEARCH ARTICLE

Enhanced charge extraction for all-inorganic perovskite solar cells by graphene oxide quantum dots modified TiO_2 layer

Yili Liu[1], Guoliang Che[1], Weizhong Cui[1], Beili Pang (✉)[1], Qiong Sun[1], Liyan Yu (✉)[1], Lifeng Dong (✉)[1,2]

1 College of Materials Science and Engineering, Qingdao University of Science and Technology, Qingdao 266042, China
2 Department of Physics, Hamline University, St. Paul, MN 55104, USA

Abstract All-inorganic cesium lead bromide ($CsPbBr_3$) perovskite solar cells have been attracting growing interest due to superior performance stability and low cost. However, low light absorbance and large charge recombination at TiO_2/$CsPbBr_3$ interface or within $CsPbBr_3$ film still prevent further performance improvement. Herein, we report devices with high power conversion efficiency (9.16%) by introducing graphene oxide quantum dots (GOQDs) between TiO_2 and perovskite layers. The recombination of interfacial radiation can be effectively restrained due to enhanced charge transfer capability. GOQDs with C-rich active sites can involve in crystallization and fill within the $CsPbBr_3$ perovskite film as functional semiconductor additives. This work provides a promising strategy to optimize the crystallization process and boost charge extraction at the surface/interface optoelectronic properties of perovskites for high efficient and low-cost solar cells.

Keywords all inorganic, perovskite solar cells, graphene oxide quantum dots, high performance, stability

1 Introduction

Perovskite solar cells (PSCs) have emerged as a pioneer in the area of future solar cells owing to their outstanding photovoltaic performance and low cost [1–5]. However, the instability would be challenging for long-term stability due to low tolerance to temperature, humidity and residual solvents [6,7]. Recently, inorganic perovskites have attracted great attention because of their thermal stability and enhanced moisture resistant compared to hybrid counterparts [8–11]. The resultant inorganic $CsPbX_3$ halides are featured with high charge carrier mobility, remarkable light absorption and considerable stability against humidity and heat [12–16].

To increase power conversion efficiency (*PCE*) of the $CsPbBr_3$ device, a challenging and promising route is to optimize the crystallization process and adjust interfacial energy-level differences to improve charge extraction [17,18]. Since graphene-based derivatives possess excellent electronic properties, they have been investigated as candidates for doping materials and interfacial materials. Functional additives could tailor grain boundary trap states to annihilate defect states [19]. For example, polyaniline/graphite composites incorporated into carbon electrode can not only regulate work function, but also enhance back electrode's ability to extract holes [20]. Kırbıyık et al. [21] introduced nitrogen doped carbon quantum dots into organic perovskite precursor to decrease voids or defects in perovskite domains for controlling the crystallization process to prevent the aggregation of perovskite. Yuan et al. [22] presented an enhanced *PCE* of 7.93% by inserting quantum dots between the perovskite absorption layer and transport layer. However, the cumbersome preparation and poor repeatability for devices is inevitable, which is an obstacle for practical applications.

Herein, we optimized a strategy to use GOQDs with abundant C and O active sites for participating in the crystallization of perovskite film to improve electron extraction performances and effectively reduce the possibility of deep charge traps forming at grain boundaries. The $CsPbBr_3$ PSCs with GOQDs demonstrated better performances than other devices reported in literature. The performance comparison of $CsPbBr_3$ PSCs with other graphene materials is shown in Table S1 (cf. Electronic Supplementary Material, ESM). The GOQDs

Received June 9, 2022; accepted August 20, 2022

E-mails: pangbl@qust.edu.cn (Pang B.), liyanyu@qust.edu.cn (Yu L.), donglifeng@qust.edu.cn (Dong L.)

were prepared by exfoliation method and dispersed evenly in *N*,*N*-dimethylformamide, which was deposited at the interface of TiO_2/$CsPbBr_3$ to optimize crystal size and accelerate electron extraction. We fabricated all-inorganic PSCs with a structure of fluorine-doped tin oxide (FTO)/TiO_2/GOQDs@$CsPbBr_3$/carbon without hole transport layer (HTL). This surface modification method could achieve a high *PCE* up to 9.16%, which is easier to operate and has excellent repeatability. These findings indicate that graphene-based derivatives can not only be used as interface modification materials, but can also be partially doped into the crystalline layer, affecting crystalline morphology and passivation defects for high-performance PSCs.

2 Experimental

2.1 Materials

CsBr (≥ 99.99%) and $PbBr_2$ (≥ 99.99%) were purchased from Xi'an p-OLED. *N*,*N*-dimethylformamide (DMF, ≥ 99.9%), $TiCl_4$ (≥ 99.5%), and ethanol were bought from Aladdin. TiO_2 paste (18 NR) was purchased from Dyesol (Australia). All chemicals were used without any further purification.

2.2 Synthesis of GOQDs

The GOQDs were synthesized via hydrothermal treatment of graphene oxide material, which was prepared following Hummers' method reported in our previous study [23,24]. First, 100 mg graphene oxide was ground for half an hour and then transferred to 10 mL of DMF for 60 min ultrasonic dispersion to obtain a homogeneous solution, and hydrothermal reaction was carried out at 200 °C for 5 h and cooling to room temperature naturally. The product was filtered by 0.02 μm microporous membrane and a brown solution was obtained, the black precipitate was discarded.

2.3 Fabrication of perovskite solar cell devices

All fabrication processes were performed under air atmosphere. The FTO glass substrates were etched for desirable patterns and purified by distilled water, acetone, 2-propanol, and ethanol, respectively. The compact TiO_2 layer and mesoporous TiO_2 layer were spin-coated onto FTO substrate, respectively [25]. Then, the TiO_2 layers were treated in $TiCl_4$ aqueous solution at 75 °C for 30 min, and annealed at 450 °C for 30 min in air. The GOQDs in DMF solution was deposited onto the TiO_2 layer at 2500 $r \cdot min^{-1}$ for 30 s, followed by a heating at 90 °C for 30 min. This step was repeated for three times to get more GOQDs between TiO_2 and perovskite film. The perovskite film was acquired by using multistep solution-processed method. $PbBr_2$ in DMF solution was covered on the above surface at 3500 $r \cdot min^{-1}$ for 30 s and annealed at 90 °C for 30 min. Then, methanol solution of CsBr was spin-coated on top of the dried $PbBr_2$ at 2000 $r \cdot min^{-1}$ for 30 s and the film was heated at 250 °C for 5 min. Finally, a carbon back-electrode coated on the perovskite layer by blade coating with an active area of 0.09 cm^2 and then heated at 120 °C for 20 min.

2.4 Characterizations

X-ray diffraction patterns were obtained using X-ray diffractometer (XRD, Rigaku, D/MAX-2500/PC). The morphology of the perovskite films was characterized by scanning electron microscopy (SEM, JEOL-JSM 6700F). The GOQDs were characterized by transmission electron microscopy (TEM, JEM-2100F) and atomic force microscope (AFM, Multimode8, Bruker). The steady photoluminescence (PL) and time-resolved photoluminescence (TR-PL) were measured using the FLS1000. The photocurrent density–voltage (*J*–*V*) curves were measured by using an electrochemical workstation (CHI750e) under a solar simulator (Newport 96000, USA) with the irradiation of 100 $mW \cdot cm^{-2}$ (AM 1.5). The dark *J*–*V* curves were measured at a scan rate of 10 $mV \cdot s^{-1}$ (–1.6 to 1.6 V). The spectral response was obtained by an incident photon-to-current collection efficiency measurement system (EQE, Newport Power Meter 2936-C). The absorption spectra were analyzed by an ultraviolet-visible spectrophotometer (UV-3900, HITACHI) at room temperature. X-ray photoelectron spectroscopy (XPS) was performed (ESCALAB Xi^+, ThermoFisher). In our work, all fabrication processes and measurements were carried out under ambient condition.

3 Results and discussion

The schematic illustration of constructing an all-inorganic PSC device is presented in Scheme 1. Both c-TiO_2 and m-TiO_2 layers were spin-coated onto the FTO substrate. To realize effective charge extraction, a GOQDs solution was dropped onto the dried TiO_2 layer. The $CsPbBr_3$ film was prepared by a solution-process method [26]. Finally, conductive carbon slurry was applied to cover solar cell by a doctor-blade method. The $CsPbBr_3$ device with GOQDs consists of a layered structure of FTO/TiO_2/GOQDs@$CsPbBr_3$/carbon.

We used TEM, UV–Vis and AFM to analyze the structure, optical properties, and morphology of GOQDs (Fig. 1). Figure 1(a) presents the morphology of GOQDs with a size of circa 4 ± 1 nm, and high resolution TEM image (Fig. 1(b)) displays the interlayer spacing of 0.3 nm. There are characteristic GOQD peaks at the

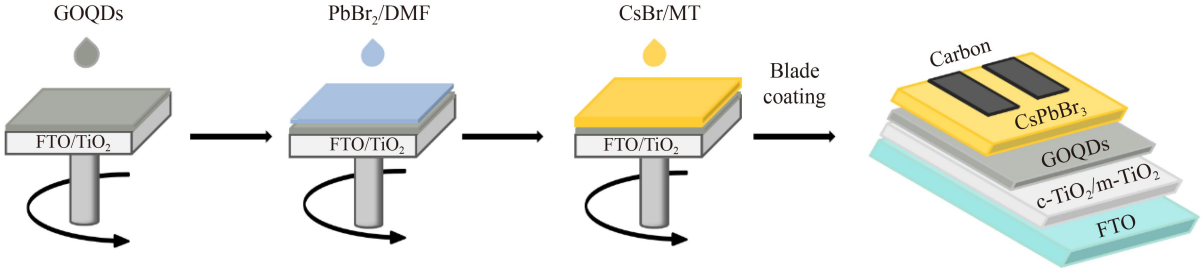

Scheme 1 Schematic illustration for constructing a PSC device.

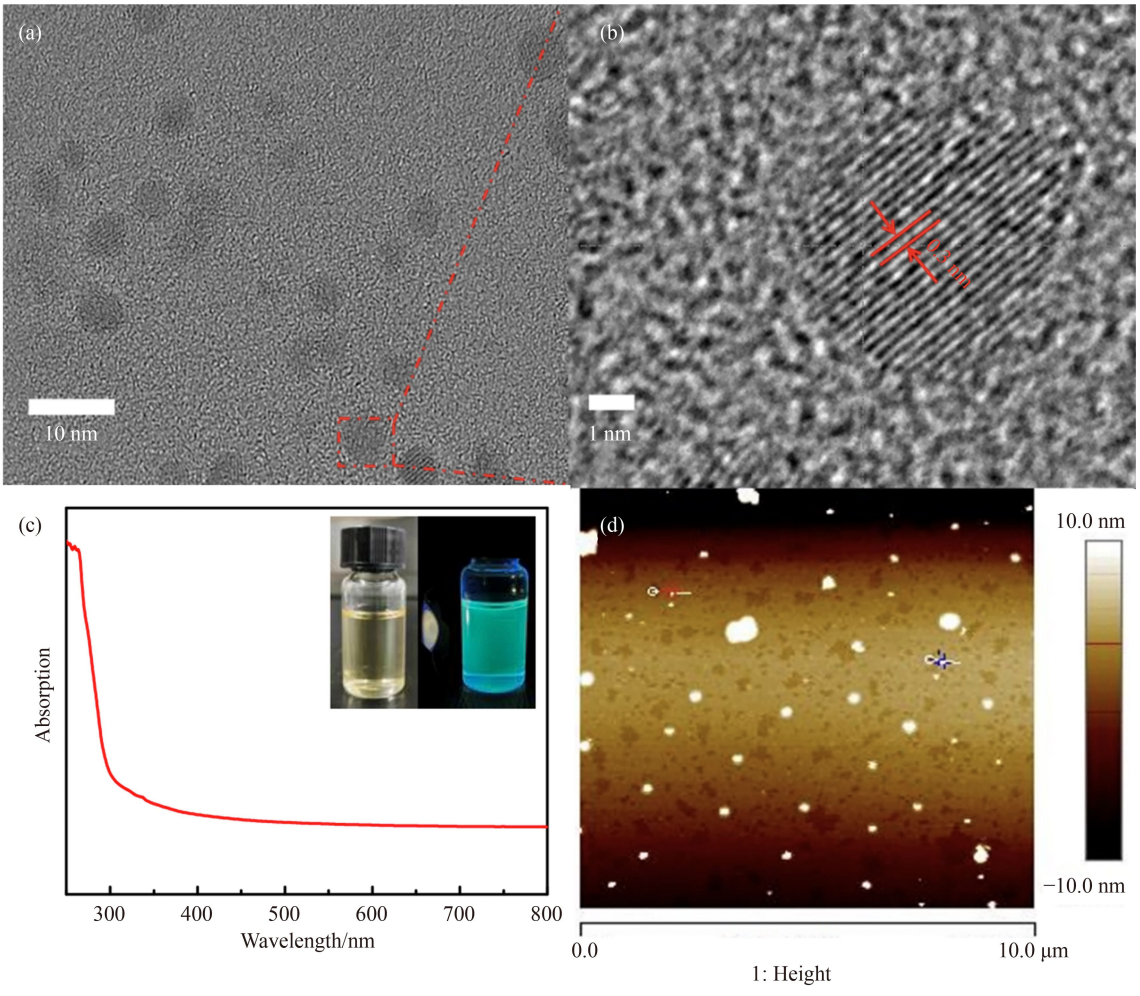

Fig. 1 TEM images of GOQDs at (a) low and (b) high magnifications; (c) the optical properties of GOQDs (inset: photographs taken under room light and 365 nm UV light); (d) AFM image of GOQDs.

UV–Vis absorption spectrum (Fig. 1(c)) because of edge effects and strong quantum confinement [27]. Meanwhile the GOQDs reveal great dispersion in methanol solution with a bright blue–green color under the illumination of 365 nm wavelength (inset of Fig. 1(c)). AFM image (Fig. 1(d)) shows that the synthesized GOQDs were well dispersed without apparent agglomeration and had a relatively uniform size distribution between 2 and 5 nm. The AFM image confirms that GOQD particles do not react easily with each other and can be stable in DMF at room temperature for two weeks.

The device structure, SEM cross section image, energy bandgap diagram, and photoelectronic properties are shown in Fig. 2 and Table 1. The devices were made of a stack of FTO/TiO_2/GOQDs@$CsPbBr_3$/carbon as presented in Fig. 2(a). Figure 2(b) shows the cross-sectional SEM image of the device based on GOQDs/perovskite layers, which demonstrates that the mesoporous titanium dioxide layer and GOQDs have cross contact with the perovskite crystal layer and they are in a situation of mutual penetration. Compared to the pristine perovskite (Fig. S1, cf. ESM), the introduction of GOQDs can tailor the crystallization of $CsPbBr_3$ and increase the size of perovskite $CsPbBr_3$ in all dimensions.

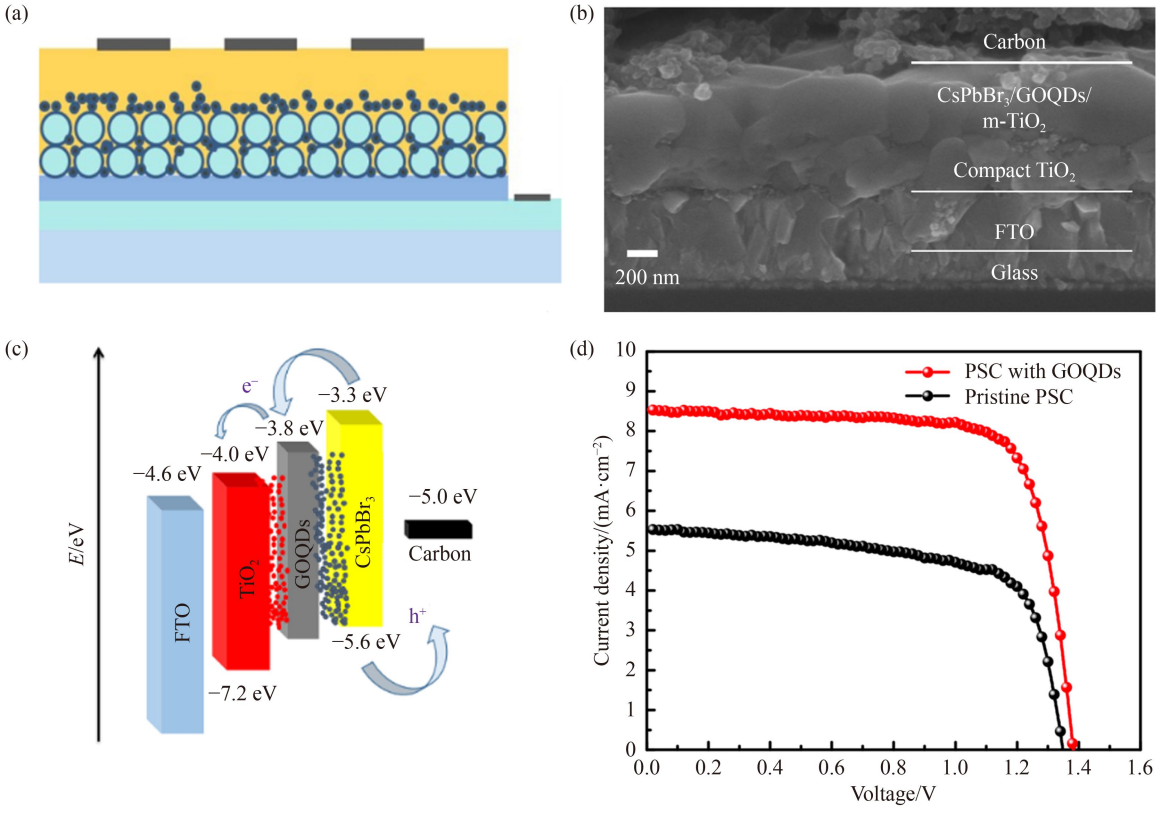

Fig. 2 (a) Schematic representation of a typical full device structure; (b) cross-sectional SEM image of a complete photovoltaic device; (c) the energy band alignment relative to vacuum; (d) current density-voltage curves for the best-performing solar cells.

Table 1 Photovoltaic parameters of $CsPbBr_3$ fabricated with or without GOQDs

PSC device	J_{sc}/(mA·cm^{-2})	V_{oc}/V	*FF*/%	*PCE*/%
Pristine PSC	6.23	1.26	69.2	5.43
PSC with GOQDs	8.54	1.38	77.6	9.16

The relative energy levels of different layers are shown in Fig. 2(c). Cyclic voltammetry was used to characterize energy level of GOQDs as described in the references [28,29]. This finding also illustrates the beneficial effect of GOQDs in promoting the transfer of electrons from the perovskite absorber to the current collector [30]. Figure 2(d) depicts the *J*–*V* curves of pristine PSC and PSC with GOQDs under AM 1.5G illumination, and Table 1 shows their corresponding photovoltaic parameters. Without GOQDs, the PSC device exhibits a *PCE* of 5.43% with V_{oc} = 1.26 V, J_{sc} = 6.23 mA·cm^{-2}, and *FF* = 69.2%. With the introduction of GOQDs to induce crystallization and modify the TiO_2/$CsPbBr_3$ interface, the *PCE*, V_{oc}, J_{sc} and *FF* are improved to 9.16%, 1.38 V, 8.54 mA·cm^{-2}, and 77.6%, respectively. All the photovoltaic parameters are enhanced, which further confirms that the presence of GOQDs can lead to high crystallinity of $CsPbBr_3$ and efficient electron extraction at the TiO_2/$CsPbBr_3$ interface [31]. The TRPL spectra (Fig. S2, cf. ESM) and related parameters (Table S2, cf. ESM) further confirm the reduced non-radiative recombination of photo-generated carriers in the perovskite film with GOQDs owing to the enhanced PL decay lifetime [32]. The charge carrier lifetime could be determined by fitting the decay curves by bi-exponential function. The average lifetimes were calculated to be around 1.79 and 4.29 ns for perovskite films with and without GOQDs, respectively. The decreased carrier lifetime can be attributed to faster charge carrier transfer process from the perovskite to the TiO_2 layer, which is helpful for efficient charge transport and extraction. This is related to the improved interface contact properties due to enhanced conductivity and reduced defects or traps because of GOQD passivation. In addition, as shown in the Hall Effect parameter (Table S3, cf. ESM), the presence of GOQDs can increase carrier mobility.

The XRD, XPS and SEM images of the films are demonstrated in Fig. 3 to validate the existence of GOQDs. Figure 3(a) presents the XRD patterns of various perovskite films. For the $CsPbBr_3$ films were prepared from fewer spin-coating cycles (< 6 cycle), three diffraction peaks appear at 11.7°, 29.4° and 33.3° corresponding to the $PbBr_2$-riched phase of $CsPb_2Br_5$. The distinctive peaks at 15.5°, 21.6° and 30.7° correspond to the (100), (110) and (200) planes of $CsPbBr_3$, respectively [33]. When repeated processes are up to 6 cycles, the intensities of the characteristic peaks at the two crystal planes (100) and (110) are higher than those under fewer spin-coating cycles and the $CsPb_2Br_5$-

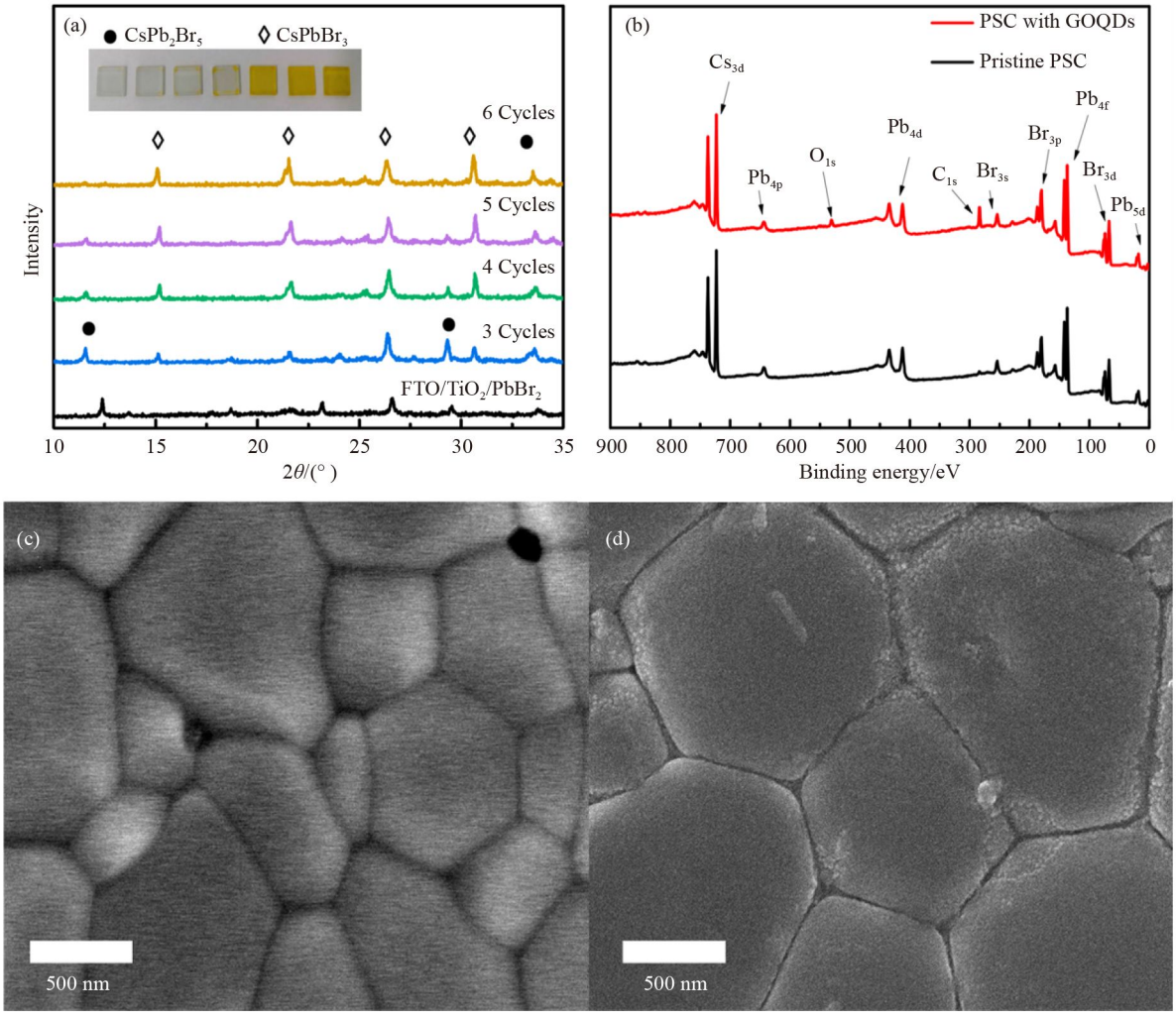

Fig. 3 (a) XRD spectra of perovskite films with various multistep solution-processes; (b) XPS of the PSCs with and without GOQDs; SEM images of perovskite film (c) without GOQDs and (d) with GOQDs.

phase generation is inhibited, indicating a change from $CsPb_2Br_5$ to $CsPbBr_3$ phase occurs with different numbers of CsBr spin coating, which implies that a high-purity $CsPbBr_3$ layer is produced. Meanwhile, as shown in Fig. S3 (cf. ESM), the introduction of GOQDs does not change the main diffraction peaks of $CsPbBr_3$ crystals, but the crystallinity can be improved with enhanced diffraction intensity of the (110) plane. In particular, the GOQDs-$CsPbBr_3$ film achieves better degree of crystallinity because of increased diffraction intensity at 21.6°, and suppresses the growth of $CsPb_2Br_5$ crystals due to weaker diffraction peak at 29.4°. As a result, the films with added GOQDs have a higher crystallinity than the pristine $CsPbBr_3$ film. XPS measurements (Fig. 3(b)) indicate the contents of C and O elements in the $FTO/TiO_2/CsPbBr_3$ and $FTO/TiO_2/GOQDs@CsPbBr_3$ structure, which provides important evidence for the existence of GOQDs in the crystalline layer. In the top-view SEM images for the pristine perovskite film and the modified perovskite film, similar morphologies are observed (Figs. 3(c) and 3(d)). Some voids were observed at the grain boundary in Fig. 3(c), which is the main manifestation of the defect problem of the perovskite layer [19]. Figure 3(d) shows that the grains of the $CsPbBr_3$ film with GOQDs are more unambiguous and legible than those of the pristine $CsPbBr_3$ film. The average grain size of the $CsPbBr_3$ film with GOQDs is circa 1.22 μm with much reduced grain boundaries. The increased grain size could enhance the crystallinity and restrain the structural defects associated with the pinholes. This also explains that GOQDs with plentiful carbon active sites participate in the crystallization of perovskite film. Electron mobility can be enhanced by increasing the crystallinity and purity of the perovskite film and reducing the intermediate phase, which improves solar cell device performances [34].

To investigate the effects of adding GOQDs on the photovoltaic performance of solar cells, we analyzed the bandgap and photoelectrical properties of the devices as presented in Fig. 4. Photophysical characteristics of different $CsPbBr_3$ films were examined. Figure 4(a) shows the UV–Vis absorption spectra of fabricated films,

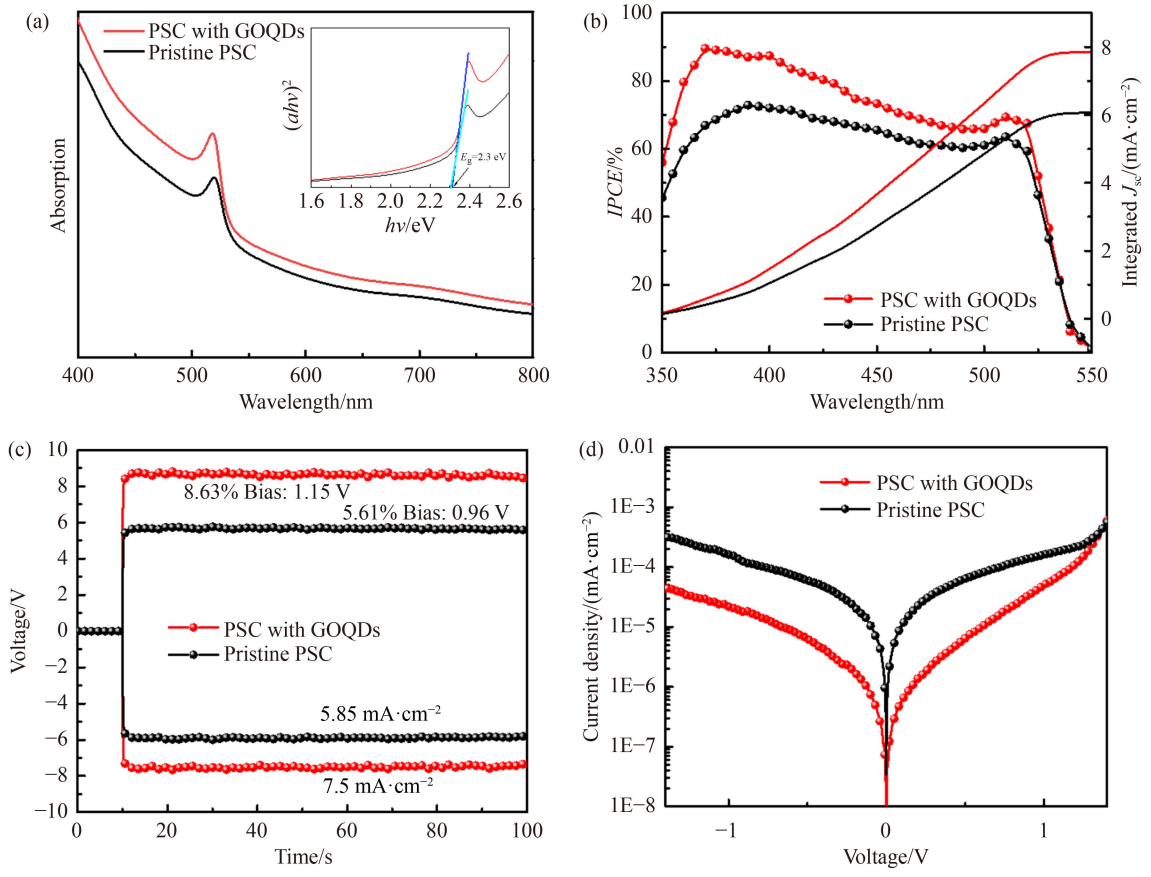

Fig. 4 (a) UV–Vis absorption spectra of $CsPbBr_3$ films (inset: $(ahv)^2$ versus hv plot); (b) *IPCE* spectra, (c) steady power output, and (d) *J–V* curves in dark of PSCs with and without GOQDs.

which intensity is highly related to the film thickness. The perovskite-structured $CsPbBr_3$ film shows an absorption onset at 515 nm and weak absorption beyond 540 nm, which is mainly attributed to its large bandgap of 2.3 eV. The film modified by GOQDs does not change absorption property of the film and absorbs the light effectively that has not been fully absorbed by blank perovskite ranging from 540 to 800 nm. The illustrated curve (inset of Fig. 4(a)) shows the relationship between photo energy (hv) and $(ahv)^2$, which is obtained from the absorption spectrum. Based on the Kubelka–Munk equation, the optical bandgap (E_g) of the $CsPbBr_3$ is 2.3 eV, which is compliance with those previously reported [8]. It is interesting that the PL peak intensity of TiO_2 film was reduced by 24% with the introduction of GOQDs (Fig. S4, cf. ESM). This indicates that trap states were effectively passivated as a result of improved TiO_2 film quality with the presence of GOQDs. Meanwhile, it indicates that efficient PL quenching occurred because of better charge transfer between electron transport layer (TiO_2) and perovskite film [35]. According to the UV–Vis and UPS curves (Fig. S5, cf. ESM), the valence band maximum and conduction band minimum of the TiO_2 electron transport layer with GOQDs are −7.2 and −3.92 eV, respectively. The incident photon-to-current efficiency (*IPCE*) and integrated current density as a function of wavelength are shown in Fig. 4(b), which match well with the values from the *J–V* curve. Therefore, introducing GOQDs as an interfacial modification layer can suppress the recombination of interfacial radiation and enhance charge transfer capability.

For the $CsPbBr_3$-based devices, the *IPCE* values were higher than those of the control PSC while all integrated J_{sc} was almost identical to the J_{sc} values extracted from the *J–V* measurements. Consistent power output curves were recorded at bias voltage at the maximum power point to verify the validity of the power output improvement, as shown in Fig. 4(c). Continuous power output, output current density and *PCE* for 300 s or more are consistent to the corresponding values from the *J–V* measurement, which ensures good reliability of the PV performance analysis. To detail the charge transport mechanism within the device, we measured *J–V* data in the dark, as shown in Fig. 4(d). A logarithmic plot of current density versus voltage (log J versus V) was investigated and as shown in the plot, the leakage current of the doped perovskite device is clearly lower, which is consistent with the previous *J–V* tests. According to the literature [36–38], the ideal factors n_{id} of the devices with and without GOQDs are respectively 1.5 and 1.6 by using the slope of V and log J functions. The dark *J–V* curves

reveal that non-zero slopes are an inevitable consequence of charge-carrier mobility. Low mobility represented by high slope causes an apparent shunt resistance (R_{sh}). Meanwhile, it appears that the GOQDs-added devices show smaller leakage current, suggesting higher shunt resistance (R_s) of the device.

The long-term stability of all-inorganic PSC devices with and without GOQDs were analyzed by the variation of *J*–*V* curves with the storing days (Fig. 5). The devices were stored at ambient condition with relative humidity of about 35% without any encapsulation. The XRD patterns in Fig. S6 (cf. ESM) show that the $CsPbBr_3$ film with GOQDs keeps high crystallinity after 8 d in atmosphere. There is no obvious crystal phase change after eight days of storage. The peaks at 30.4° and 27.8° correspond to $CsPbBr_3$ and $CsPb_2Br_5$, and their diffraction intensities are slightly increased, which may be one of the reasons for the improved device performance [39]. After 40 d, the *PCE* of the devices without GOQDs decreases by 25% at ambient condition (Fig. 5). In contrast, the devices with GOQDs maintain 94% of initial *PCE* under the same experimental conditions, reflecting a remarkable long-term stability. This increased stability derived from introducing GOQDs can be attributed to the protective effect and the surface defect.

Sixty-two devices were prepared and measured under the optimized conditions to study the reproducibility of the PSCs with GOQDs. The statistical data of the device performance parameters are shown in Fig. 6. The averages of *PCE*, *FF*, V_{oc} and J_{sc} are 8.9%, 75%, 1.38 V and 8.5 mA·cm^{-2}, respectively and close to the best device parameters, indicating the device with GOQDs has high reproducibility, which is mainly attributed to the high-quality perovskite film.

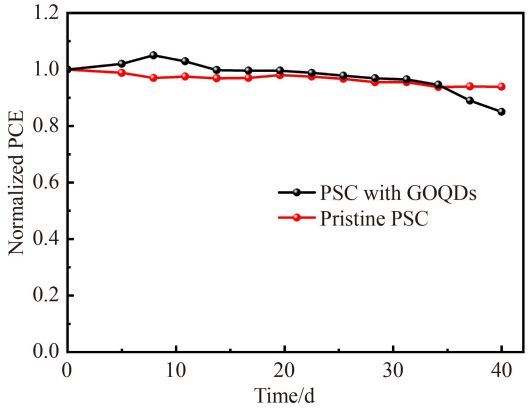

Fig. 5 Long-term stability of un-encapsulated $CsPbBr_3$ PSCs with or without GOQDs layer.

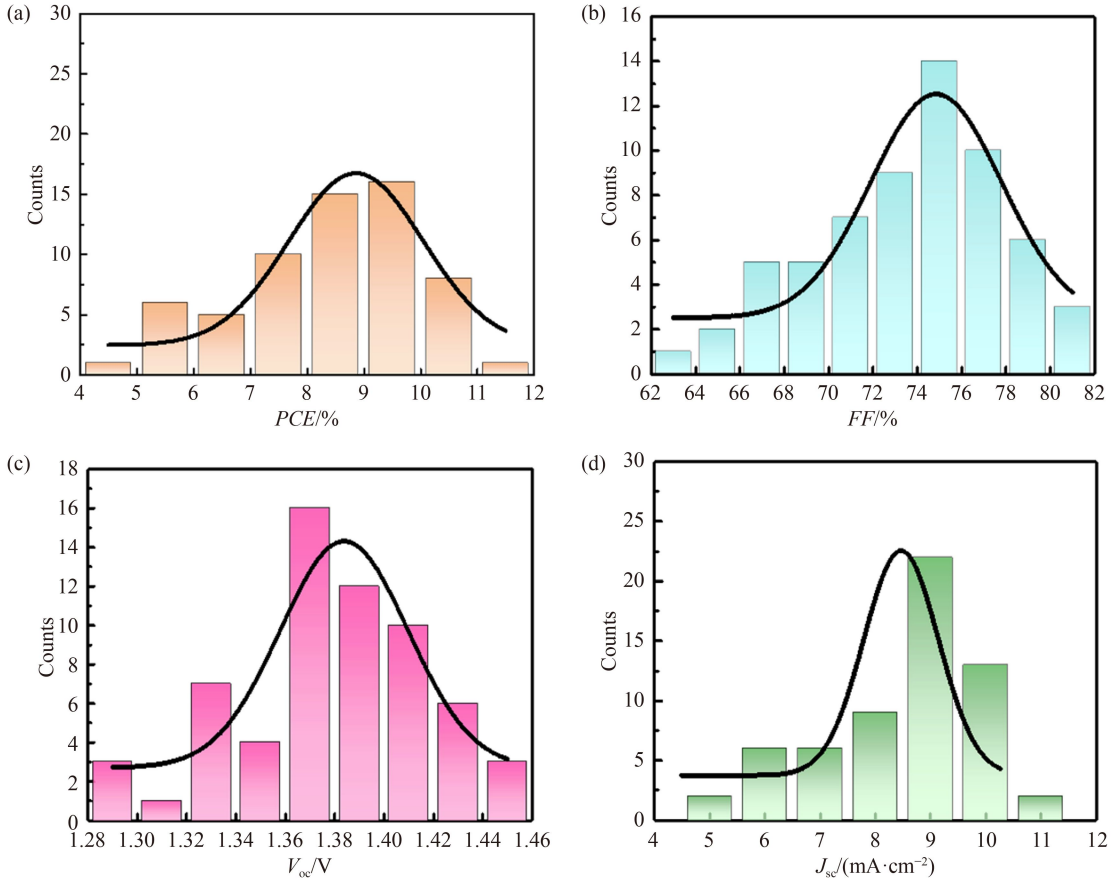

Fig. 6 The normal distribution of 62 devices fabricated with PSCs.

4 Conclusions

In this work, highly dispersible GOQDs nanoparticles were used as interface modification in $CsPbBr_3$ perovskite. We presented the use of GOQDs at TiO_2/$CsPbBr_3$ interface as a valid pathway to accomplish highly efficient defect passivation carbon-based HTL-free $CsPbBr_3$ PSCs, thereby achieving a prominent gain in device performance. GOQDs with compatible energy level regulates the crystallization and passivate the perovskite trap states, which is beneficial to collect electrons efficiently. Arising from promoting charge extraction, the GOQDs-treated PSCs without hole transport layer made by spin-coating obtained a higher output power conversion efficiency of 9.16% than 5.56% of the pristine device. This modified approach provides a valid and low-cost method for all-inorganic PSCs, opening up new pathway for future development of solar cells.

Acknowledgements This work was partially supported by the National Natural Science Foundation of China (Grant Nos. 21776147, 21905153 and 61604086), the Qingdao Municipal Science and Technology Bureau (Grant No. 19-6-1-91-nsh) and A Project of Shandong Province Higher Educational Science and Technology Program (Grant No. J17KA013). Lifeng Dong also thanks financial support from the Malmstrom Endowed Fund at Hamline University.

Electronic Supplementary Material Supplementary material is available in the online version of this article at https://dx.doi.org/10.1007/s11705-022-2238-z and is accessible for authorized users.

References

1. Min H, Kim M, Lee S U, Kim H, Sang I S. Efficient, stable solar cells by using inherent bandgap of α-phase formamidinium lead iodide. Science, 2019, 366(6466): 749–753
2. Cai Y Y, Zhang Z B, Zhou Y, Liu H, Qin Q Q, Lu X B, Gao X S, Shui L L, Wu S J, Liu J M. Enhancing the efficiency of low-temperature planar perovskite solar cells by modifying the interface between perovskite and hole transport layer with polymers. Electrochimica Acta, 2018, 261: 445–453
3. Zhu C T, Yang Y, Lin F Y, Luo Y, Ma S P, Zhu L, Guo X Y. Electrodeposited transparent PEDOT for inverted perovskite solar cells: improved charge transport and catalytic performances. Rare Metals, 2021, 40(9): 2402–2414
4. Wang Y Q, Yang L, Chunxiang D A, Gang C, Ai J L, Wang X F. Spray-coated SnO_2 electron transport layer with high uniformity for planar perovskite solar cells. Frontiers of Chemical Science and Engineering, 2021, 15(1): 180–186
5. Xia Y R, Zhao C, Zhao P Y, Mao L Y, Ding Y C, Hong D C, Tian Y X, Yan X S, Jin Z. Pseudohalide substitution and potassium doping in $FA_{0.98}K_{0.02}Pb(SCN)_2I$ for high-stability hole-conductor-free perovskite solar cells. Journal of Power Sources, 2021, 494(15): 229781
6. Deretzis I, Smecca E, Mannino G, La Magna A, Miyasaka T, Alberti A. Stability and degradation in hybrid perovskites: is the glass half-empty or half-full? Journal of Physical Chemistry Letters, 2018, 9(11): 3000–3007
7. Yang W S, Park B W, Jung E H, Jeon N J, Kim Y C, Lee D U, Shin S S, Seo J, Kim E K, Noh J H, Seok S I. Iodide management in formamidinium-lead-halide-based perovskite layers for efficient solar cells. Science, 2017, 356(6345): 1376–1379
8. Liang J, Wang C, Wang Y, Xu Z, Lu Z, Ma Y, Zhu H, Hu Y, Xiao C, Yi X, Zhu G, Lv H, Ma L, Chen T, Tie Z, Jin Z, Liu J. All-inorganic perovskite solar cells. Journal of the American Chemical Society, 2016, 138(49): 15829–15832
9. Kulbak M, Gupta S, Kedem N, Levine I, Bendikov T, Hodes G, Cahen D. Cesium enhances long-term stability of lead bromide perovskite-based solar cells. Journal of Physical Chemistry Letters, 2016, 7(1): 167–172
10. Kulbak M, Cahen D, Hodes G. How important is the organic part of lead halide perovskite photovoltaic cells efficient $CsPbBr_3$ cells? Journal of Physical Chemistry Letters, 2015, 6(13): 2452–2456
11. Liang J, Zhu G Y, Wang C X, Zhao P Y, Wang Y R, Hu Y, Ma L B, Tie Z X, Liu J, Jin Z. An all-inorganic perovskite solar capacitor for efficient and stable spontaneous photocharging. Nano Energy, 2018, 52: 239–245
12. Liang J, Liu J, Jin Z. All-inorganic halide perovskites for optoelectronics: progress and prospects. Solar RRL, 2017, 1(10): 1700086
13. Liang J, Wang C X, Zhao P Y, Lu Z P, Ma Y, Xu Z R, Wang Y R, Zhu H F, Hu Y, Zhu G Y, Ma L, Chen T, Tie Z, Liu J, Jin Z. Solution synthesis and phase control of inorganic perovskites for high-performance optoelectronic devices. Nanoscale, 2017, 9(33): 11841–11845
14. Chen C Y, Lin H Y, Chiang K M, Tsai W L, Huang Y C, Tsao C S, Lin H W. All-vacuum-deposited stoichiometrically balanced inorganic cesium lead halide perovskite solar cells with stabilized efficiency exceeding 11%. Advanced Materials, 2017, 29(12): 1605290
15. Rong Y G, Liu L F, Mei A Y, Li X, Han H W. Beyond efficiency: the challenge of stability in mesoscopic perovskite solar cells. Advanced Energy Materials, 2015, 5(20): 1501066
16. Liang J, Zhao P, Wang C, Wang Y, Hu Y, Zhu G, Ma L, Liu J, Jin Z. $CsPb_{0.9}Sn_{0.1I}Br_2$ based all-inorganic perovskite solar cells with exceptional efficiency and stability. Journal of the American Chemical Society, 2017, 139(40): 14009–14012
17. Zhang L, Zhang X Z, Xu X X, Tang J, Wu J H, Lan Z. CH_3NH_3Br additive for enhanced photovoltaic performance and air stability of planar perovskite solar cells prepared by two-step dipping method. Energy Technology, 2017, 5(10): 1887–1894
18. Li Y, Duan J, Yuan H, Zhao Y, He B, Tang Q. Lattice modulation of alkali metal cations doped $Cs_{1-x}R_xPbBr_3$ halides for inorganic perovskite solar cells. Solar RRL, 2018, 2(10): 1800164
19. Niu T, Lu J, Munir R, Li J, Barrit D, Zhang X, Hu H, Yang Z, Amassian A, Zhao K, Liu S F. Stable high-performance perovskite solar cells via grain boundary passivation. Advanced Materials, 2018, 30(16): 1706576
20. Bu F, He B L, Ding Y, Li X K, Sun X M, Duan J L, Zhao Y Y, Chen H Y, Tang Q W. Enhanced energy level alignment and hole

extraction of carbon electrode for air-stable hole-transporting material-free $CsPbBr_3$ perovskite solar cells. Solar Energy Materials and Solar Cells, 2020, 205: 110267

21. Kırbıyık Ç, Toprak A, Başlak C, Kuş M, Ersöz M. Nitrogen-doped CQDs to enhance the power conversion efficiency of perovskite solar cells via surface passivation. Journal of Alloys and Compounds, 2020, 832: 154897
22. Yuan H W, Zhao Y Y, Duan J L, He B L, Jiao Z B, Tang Q W. Enhanced charge extraction by setting intermediate energy levels in all-inorganic $CsPbBr_3$ perovskite solar cells. Electrochimica Acta, 2018, 279: 84–90
23. Pang B L, Dong L F, Ma S, Dong H Z, Yu L Y. Performance of FTO-free conductive graphene-based counter electrodes for dye-sensitized solar cells. RSC Advances, 2016, 6(47): 41287–41293
24. Wang Y Y, Bao X C, Pang B L, Zhu Q Q, Wang J Y, Zhu D Q, Yu L Y, Yang R Q, Dong L F. Solution-processed functionalized reduced graphene oxide—an efficient stable electron buffer layer for high-performance solar cells. Carbon, 2018, 131: 31–37
25. Najafi L, Taheri B, Martin-Garcia B, Bellani S, Di Girolamo D, Agresti A, Oropesa-Nunez R, Pescetelli S, Vesce L, Calabro E, Prato M, Del Rio Castillo A E, Di Carlo A, Bonaccorso F. MoS_2 quantum dot/graphene hybrids for advanced interface engineering of a $CH_3NH_3PbI_3$ perovskite solar cell with an efficiency of over 20%. ACS Nano, 2018, 12(11): 10736–10754
26. Duan J, Zhao Y, He B, Tang Q. Simplified perovskite solar cell with 4.1% efficiency employing inorganic $CsPbBr_3$ as light absorber. Small, 2018, 14(20): 1704443
27. Xu S J, Li D, Wu P Y. One-pot, facile, and versatile synthesis of monolayer $MosS_2/WS_2$ quantum dots as bioimaging probes and efficient electrocatalysts for hydrogen evolution reaction. Advanced Functional Materials, 2015, 25(7): 1127–1136
28. Cardona C M, Li W, Kaifer A E, Stockdale D, Bazan G C. Electrochemical considerations for determining absolute frontier orbital energy levels of conjugated polymers for solar cell applications. Advanced Materials, 2011, 23(20): 2367–2371
29. Li Y, Hu Y, Zhao Y, Shi G, Deng L, Hou Y, Qu L. An electrochemical avenue to green-luminescent graphene quantum dots as potential electron-acceptors for photovoltaics. Advanced Materials, 2011, 23(6): 776–780
30. Zhu Z, Ma J, Wang Z, Mu C, Fan Z, Du L, Bai Y, Fan L, Yan H, Phillips D L, Yang S. Efficiency enhancement of perovskite solar cells through fast electron extraction: the role of graphene quantum dots. Journal of the American Chemical Society, 2014, 136(10): 3760–3763
31. Moriya M, Hirotani D, Ohta T, Ogomi Y, Shen Q, Ripolles T S, Yoshino K, Toyoda T, Minemoto T, Hayase S. Architecture of the interface between the perovskite and hole-transport layers in perovskite solar cells. ChemSusChem, 2016, 9(18): 2643
32. Yang Y, Peng H R, Liu C, Arain Z, Ding Y, Ma S, Liu X L, Hayat T, Alsaedi A, Dai S. Bi-functional additive engineering for high-performance perovskite solar cells with reduced trap density. Journal of Materials Chemistry A: Materials for Energy and Sustainability, 2019, 7(11): 6450–6458
33. Duan J, Zhao Y, He B, Tang Q. High-purity inorganic perovskite films for solar cells with 9.72% efficiency. Angewandte Chemie International Edition, 2018, 57(14): 3787–3791
34. Zhao Y, Tan H, Yuan H, Yang Z, Fan J Z, Kim J, Voznyy O, Gong X, Quan L N, Tan C S, Hofkens J, Yu D, Zhao Q, Sargent E H. Perovskite seeding growth of formamidinium-lead-iodide-based perovskites for efficient and stable solar cells. Nature Communications, 2018, 9(1): 1607
35. Chang J, Zhu H, Li B, Isikgor F H, Hao Y, Xu Q, Ouyang J. Boosting the performance of planar heterojunction perovskite solar cell by controlling the precursor purity of perovskite materials. Journal of Materials Chemistry A: Materials for Energy and Sustainability, 2016, 4(3): 887–893
36. Mu X H, Yu X G, Xu D K, Shen X L, Xia Z H, He H, Zhu H Y, Xie J S, Sun B Q, Yang D R. High efficiency organic/silicon hybrid solar cells with doping-free selective emitter structure induced by a WO_3 thin interlayer. Nano Energy, 2015, 16: 54–61
37. Liu X Y, Tan X H, Liu Z Y, Sun B, Li J J, Xi S, Shi T L, Liao G G. Sequentially vacuum evaporated high-quality $CsPbBr_3$ films for efficient carbon-based planar heterojunction perovskite solar cells. Journal of Power Sources, 2019, 443: 227269
38. Bouzidi K, Chegaar M, Bouhemadou A. Solar cells parameters evaluation considering the series and shunt resistance. Solar Energy Materials and Solar Cells, 2007, 91(18): 1647–1651
39. Tong G Q, Chen T T, Li H, Qiu L B, Liu Z H, Dang Y Y, Song W T, Luis K O, Jiang Y, Qi Y B. Phase transition induced recrystallization and low surface potential barrier leading to 10.91%-efficient $CsPbBr_3$ perovskite solar cells. Nano Energy, 2019, 65: 104015